

Obliquity Constraints on the Planetary-mass Companion HD 106906 b

Marta L. Bryan ¹ ©, Eugene Chiang ¹ ©, Caroline V. Morley ² ©, Gregory N. Mace ² ©, and Brendan P. Bowler ² ©
Department of Astronomy, 501 Campbell Hall, University of California Berkeley, Berkeley, CA 94720-3411, USA; martalbryan@berkeley.edu

Department of Astronomy, The University of Texas at Austin, Austin, TX 78712, USA

Received 2021 June 15; accepted 2021 August 5; published 2021 October 27

Abstract

We constrain the angular momentum architecture of HD 106906, a 13 ± 2 Myr old system in the ScoCen complex composed of a compact central binary, a widely separated planetary-mass tertiary HD 106906 b, and a debris disk nested between the binary and tertiary orbital planes. We measure the orientations of three vectors: the companion spin axis, companion orbit normal, and disk normal. Using near-IR high-resolution spectra from Gemini/IGRINS, we obtain a projected rotational velocity of $v \sin i_p = 9.5 \pm 0.2$ km s⁻¹ for HD 106906 b. This measurement together with a published photometric rotation period implies the companion is viewed nearly pole-on, with a line-of-sight spin axis inclination of $i_p = 14^{\circ} \pm 4^{\circ}$ or $166^{\circ} \pm 4^{\circ}$. By contrast, the debris disk is known to be viewed nearly edge on. The likely misalignment of all three vectors suggests HD 106906 b formed by gravitational instability in a turbulent environment, either in a disk or cloud setting.

Unified Astronomy Thesaurus concepts: Exoplanet astronomy (486); Exoplanet formation (492); Exoplanet evolution (491); Exoplanet systems (484); High resolution spectroscopy (2096); Astrostatistics (1882)

1. Introduction

Planetary obliquity measurements inform our understanding of how planets form and evolve. A planetary obliquity is the mutual inclination between the planet's spin axis and its orbit normal. Up until last year, only solar system planets had measured obliquities. In this single system we find a wide range of orientations–Uranus is on its side, Venus is upside down, and Earth is tilted by 23°, which gives us our seasons. From these spin rates and directions we can infer planet formation histories. The terrestrial and ice giant planets likely experienced giant impacts, tidal friction, and gravitational forcing (e.g., Dobrovolskis 1980; Lissauer & Kary 1991; Laskar & Robutel 1993; Touma & Wisdom 1993; Correia 2006; Schlichting & Sari 2007; Reinhardt et al. 2020). While the spin axes of Jupiter and Saturn may have initially both been aligned with the angular momentum of the broader circumstellar disk, secular spin-orbit resonances driven by orbital migration have been invoked to explain Saturn's 27° obliquity (e.g., Ward & Hamilton 2004; Nesvorný 2018).

These processes and others can apply to exoplanets. Theoretical work shows that obliquities can be excited through secular spin-orbit resonances created by planet–planet or planet-disk interactions (e.g., Millholland & Batygin 2019; Millholland & Laughlin 2019; Li 2021). Kozai–Lidov oscillations from an external perturber can be expected to produce significant planetary and stellar obliquities (e.g., Martin et al. 2014; Storch et al. 2014). Spin axes may also be tilted at the time of formation: turbulence in self-gravitating disks is expected to produce a dispersion of spin axis directions for fragmenting clumps (Bryan et al. 2020b; Jennings & Chiang 2021).

A planet's obliquity can be constrained from three observables: the projected rotation rate $v \sin i$ of the planet, its photometric rotation period $P_{\rm rot}$, and a 3D orbit. Combining $v \sin i$, $P_{\rm rot}$, and a radius estimate yields the line-of-sight spin axis inclination of the planet, and the orbit plane gives the orbital inclination. At present, the only planets amenable to these measurements are ~25 young super-Jupiters discovered by direct imaging campaigns (e.g., Bowler 2016). Because these objects are young ($\lesssim 100 \, {\rm Myr}$ old) and massive ($\sim 10-20 \, M_{\rm Jup}$),

they are relatively bright, and their large separations from their host stars ($\gtrsim 50$ au, $\gtrsim 1''$) help ensure that their fluxes are not buried beneath the glare of their host stars. It is thus feasible to extract spectra and light curves for the planets themselves, thereby measuring $v \sin i$ and $P_{\rm rot}$.

However, it is exceptionally rare to obtain all three of these observables for a single object. To date \sim 15 planetary-mass companions (PMCs) have measured rotation rates (see Table 3 in Bryan et al. 2020a). Only companions 2M0122 b and VHS 1256-1257 b have both a measured $v \sin i$ and $P_{\rm rot}$. Some objects with measured $P_{\rm rot}$ are too faint to extract a spectrum and measure $v \sin i$. Others that have measured $v \sin i$'s do not have detectable rotational modulations in their light curves, precluding a $P_{\rm rot}$ constraint. Some of these companions, such as VHS 1256-1257 b, are so far from their host stars that constraining the 3D orbit is not feasible. Prior to this work there was only one system with all three pieces in hand.

Bryan et al. (2020b) placed the first constraint on the obliquity of a planetary-mass object outside the solar system. This study focused on the 120 Myr old system 2MASS J01225093-2439505, which comprises a 0.4 M_{\odot} host star with a 12–27 M_{Jup} companion (hereafter 2M0122 b) orbiting at 52 au (Bowler et al. 2013). Line-of-sight inclinations for the planetary spin, stellar spin, and orbital angular momentum vectors were measured using projected rotational velocities $v \sin i$'s for the star and companion, rotation periods P_{rot} 's for the star and companion, and an astrometric orbit for the companion. There is evidence that the true stellar obliquity is small and the true companion obliquity is large, although there are large uncertainties because of the unknown orientation of the spin axes in the sky plane. A promising scenario that could account for these mutual inclinations is formation via instability in a gravito-turbulent disk, wherein turbulent eddies of gas spinning in a variety of directions collapse under their own selfgravity, yielding a range of obliquities for the resulting objects (Bryan et al. 2020b; Jennings & Chiang 2021).

Here we present constraints on a second extrasolar PMC obliquity. We study HD 106906, a 13 ± 2 Myr old system with a central close binary (masses 1.37 and 1.34 M_{\odot} , orbital period

 49.233 ± 0.001 days, and eccentricity 0.669 ± 0.002), orbited by an $11.9^{+1.7}_{-0.8}~M_{\rm Jup}$ companion at a projected separation of \sim 737 au (Bailey et al. 2014; Nguyen et al 2021). This system also hosts an asymmetric debris disk with a vertically-thin eastern side that extends to over 550 au, and a vertically-thick western side that reaches a radius of \sim 370 au (Kalas et al. 2015; Lagrange et al. 2016). We seek to constrain three angular momentum vectors: the planetary spin axis, planetary orbit normal, and debris disk normal. We do not include the binary star system in our analysis as the angular momentum vectors for the binary orbit and stellar spins are unknown. While recent work has shown that close, circular binaries have orbital planes that are more likely to be aligned with the planes of their circumbinary debris disks (Czekala et al. 2019), the central binary in HD 106906 has an orbital period that is too long and an eccentricity that is too high to safely make the assumption that the binary plane and the debris disk plane are coplanar.

This paper is organized as follows. In Section 2 we describe our high-resolution spectroscopic observations with IGRINS/Gemini. Section 3 lays out measurements of the line-of-sight inclinations of the planetary spin, orbital, and disk angular momentum vectors, and gives constraints on the true 3D angles between each pair. We discuss what physical scenarios could account for these constraints in Section 4, and present our conclusions in Section 5.

2. Observations

2.1. IGRINS/Gemini High-resolution Spectroscopy

Observations of HD 106906 b with the Immersion Grating Infrared Spectrometer (IGRINS; Yuk et al. 2010; Park et al. 2014) on the Gemini South telescope (Mace et al. 2018) were completed 2020 February 04, 07, 08, 09 UT as part of program GS-2020A-Q-135 (PI: Bryan). These observations simultaneously covered H and K bands from $\sim 1.45-2.52 \,\mu\text{m}$. We observed the K = 15.5 mag companion with individual image exposure times of 1528 s. All observations were taken with a slit orientation perpendicular to the 307.3° position angle (PA) between the host star and the companion (angular separation 7."1) in order to prevent a flux gradient across the slit. On 2020 February 04 UT we acquired three pairs of AB nodded exposures, amounting to three epochs of observation in \sim 2.5 hr of on-source integration time. On the nights of 2020 February 07, 08, and 09 UT ABBA-nodded exposures were combined, producing three additional epochs. In total, there were six epochs of observation from four nights in early 2020 February.

3. Analysis

3.1. Measuring v sin i for HD 106906 b

We reduce all data with the IGRINS Pipeline Package (PLP; Lee & Gullikson 2016). The package uses AB pairs of slit-nodded spectra to sky subtract and then optimally extract the target flux. Wavelength calibration is carried out using both OH sky emission and telluric absorption from the A0V star observed immediately before or after the target. The A0V star also serves as a telluric standard, and when the target spectrum is divided by the A0V spectrum the target is corrected for both telluric absorption and the instrument profile. The final product of the PLP is a wavelength-calibrated spectrum of the target star, with flux in counts, and the corresponding signal-to-noise spectrum. While reduced spectra were produced across the

wavelength range $\sim 1.45-2.52~\mu m$, we only consider the *K*-band spectra in subsequent analyses given the low signal to noise of the *H*-band spectrum. This companion is brightest in *K* band $(1.85-2.52~\mu m)$, although we find that some *K*-band orders are also unusable due to a low signal-to-noise ratio (S/N).

Instrumental resolution and rotation both produce line broadening, and these two sources of broadening are degenerate. It is thus important to accurately measure the resolution in order to accurately measure $v \sin i$. Using observed standard star spectra, we first select four IGRINS orders spanning wavelengths 2.293-2.325, 2.236-2.267, 2.182-2.212, and $2.105-2.135 \mu m$. For each of the six epochs of data, we use the molecfit routine, which simultaneously fits a telluric model and an instrumental profile defined by a single Gaussian kernel, to the spectrum (Kausch et al. 2015; Smette et al. 2015). We take the median of these 24 instrumental resolution measurements as the instrumental resolution to use in our analysis, and the standard deviation to be the uncertainty. From this analysis we find $R = 48,599 \pm 1514$. We also check whether the resolution changes significantly within an order. We select one of the epochs taken on UT 2020 February 04, and divide each of the four orders into five parts (each \sim 400 pixels across). We find that the resulting instrumental resolution values within each order are consistent with each other and with the global resolution measurement.

In the wavelength-calibrated and telluric-corrected output spectra from the IGRINS reduction routine, we remove artifacts from strong sky lines that manifested as spikes in the data. In addition, we find that the short wavelength end of each spectrum contains less flux as the instrument blaze falls off. We cut the leftmost 20–70 pixels off of each reduced spectral order, where the cutoff value grew with increasing order number (decreasing wavelength).

With these spectra of HD 106906 b, we want to measure the amount of line broadening due to the rotational velocity. To do so, we calculate the "data" cross-correlation function (CCF) between the observed spectrum and a model atmosphere, where the model has been broadened to the instrumental resolution. We use an atmospheric model from the Sonora model grid (Marley et al. 2018, 2021; C. Morley et al. 2021, in preparation). These models are calculated assuming that the atmosphere is in radiative-convective and chemical equilibrium, following the approach of Marley et al. (1999), Saumon & Marley (2008), and Morley et al. (2012), with updated chemistry and opacities as described in (Marley et al. 2018; Marley et al. 2021, in preparation.). We assume $T_{\rm eff} = 1820 \text{ K}$ and log(g) = 4.0 for HD 106906 b, following measurements of $T_{\rm eff} = 1820 \pm 240 \text{ K} \text{ and } \log(L_{\rm bol}/L_{\odot}) = -3.65 \pm 0.08 \text{ using}$ medium resolution spectra from VLT/SINFONI (Daemgen et al. 2017), and converting $\log(L_{\rm bol}/L_{\odot})$ and system age to log(g) using hot-start evolutionary models (Burrows et al. 1997). The Sonora models generated for HD 106906 b have solar metallicity and solar carbon-to-oxygen ratio (C/O), and include silicate, iron, and corundum clouds with a sedimentation efficiency $f_{\text{sed}} = 2$ as described in Ackerman & Marley

We compare this "data" CCF to "model" CCFs, where each model is calculated by cross correlating a model atmosphere broadened by the instrumental line profile with that same model additionally broadened by some rotation rate and offset by a radial velocity (RV). We perform this comparison in a Bayesian framework using MCMC to fit for three free parameters: $v \sin i$,

RV, and instrumental resolution. We use uniform priors on $v \sin i$ and RV. For the instrumental resolution, we use a Gaussian prior with a mean of 48,599 and standard deviation of 1514 to account for uncertainties on the measured resolution.

The log-likelihood function used in our MCMC framework is given by

$$\log L = \sum_{i=1}^{n} -0.5 \left(\frac{m_i - d_i}{\sigma_i}\right)^2,\tag{1}$$

where d is the "data" CCF, m is the "model" CCF, and σ_i is the CCF error at position i. We calculate uncertainties on the "data" CCF using the jackknife resampling technique. In this case, uncertainties are given by

$$\sigma_{\text{jackknife}}^2 = \frac{(n-1)}{n} \sum_{i=1}^{n} (x_i - x)^2,$$
 (2)

where n is the total number of samples. We define a sample as one epoch of data—there are six for HD 106906 b. x_j is the "data" CCF calculated using all epochs of data except the jth epoch, and x is the "data" CCF calculated using all epochs of data.

Before undertaking a joint fit of multiple orders to determine $v \sin i$, we first consider each order in K band individually. We compute "data" CCFs for 22 orders spanning wavelengths $1.85-2.42 \mu m$ (the first three spectral orders extended to longer wavelengths than those covered by our models), and determine the significance of the peak (if present) by calculating the ratio of the peak height to the standard deviation of the CCF outside the central peak. We exclude orders with peaks with less than 5σ significance. This cut leaves us with 15 orders running from $1.99-2.42 \,\mu\mathrm{m}$ (excluded orders have significant telluric features and lower S/N spectra). We fit each order individually to get independent estimates for $v \sin i$, and find that they are consistent within their uncertainties. We then perform a joint fit, calculating a "data" CCF using all 15 orders and fitting models across that entire 1.99–2.42 μm wavelength range. The measured projected rotation rate for HD 106906 b is $v \sin i =$ 9.5 ± 0.2 km s⁻¹ (see Figures 1–3 for reference).

We now consider how our modeling assumptions could impact the measured $v\sin i$. First we test our choice of $T_{\rm eff}$ and $\log(g)$. From Daemgen et al. (2017) we have $T_{\rm eff}=1820\pm240$ K, and we converted $\log(L_{\rm bol}/L_{\odot})$ to $\log(g)=4.0\pm0.5$ using hot-start evolutionary models (Burrows et al. 1997). We take the 1σ errors on these values and generate four models: (1580 K, 3.5 dex), (1580 K, 4.5 dex), (2060 K, 3.5 dex), and (2060 K, 4.5 dex). We calculate new $v\sin i$ values with each of these models to test the possible impact of the measured uncertainties on our adopted $T_{\rm eff}$ and $\log(g)$, and found that all $v\sin i$ values were consistent with our original measurement at the $\leqslant 2\sigma$ level (see Table 1).

Another assumption we make when generating atmospheric models is a C/O. In our original model we assume a solar (0.54) C/O value, and here we test three additional ones: $0.25 \times \text{solar}$, $0.5 \times \text{solar}$, and $1.5 \times \text{solar}$. When we implement these models in our MCMC framework, we find that resulting $v \sin i$ values are consistent with the original value to $\leq 0.5\sigma$ for the subsolar C/Os, and differ by 2.3σ for the $1.5 \times \text{solar}$ model (see Table 1). While not significant, this tentative offset in $v \sin i$ due to higher C/O suggests that abundance assumptions can become important for $v \sin i$'s given our measurement precision of $0.2 \, \text{km s}^{-1}$.

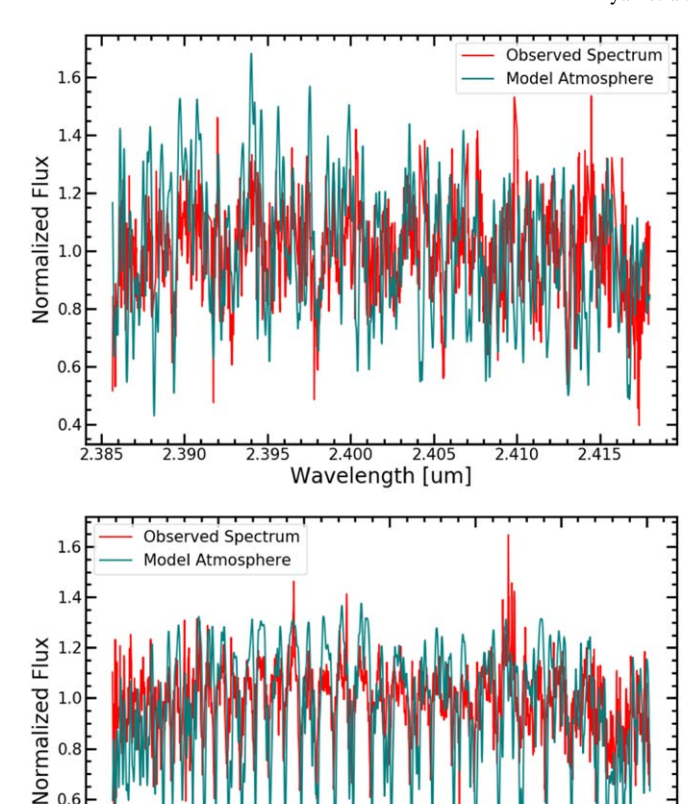


Figure 1. Orders 4 (top) and 7 (bottom) spectra for HD 106906 b (red), overplotted with a model atmosphere broadened to the best-fit rotation rate.

Wavelength [um]

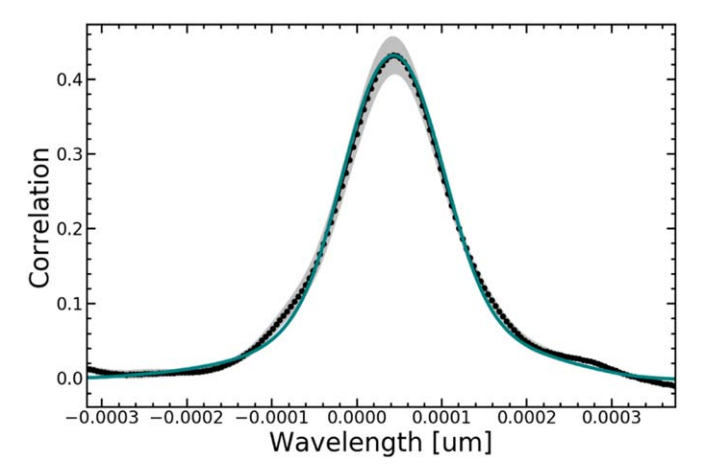


Figure 2. CCF between orders 4–19 (1.99–2.42 μ m) of the observed spectrum with a model atmosphere broadened to the instrumental resolution (black points), shown with 1σ uncertainties shaded in gray calculated using jackknife resampling technique. The CCF between a model atmosphere broadened to the instrumental resolution, and that same model additionally broadened by the best-fit rotation rate and shifted by the best-fit velocity offset is shown in teal.

Finally, we explore the impact that uncertainties in pressure broadening can have on the measured rotational velocity. Pressure broadening is a degenerate effect along with instrumental broadening and rotational line broadening-higher-pressure broadening

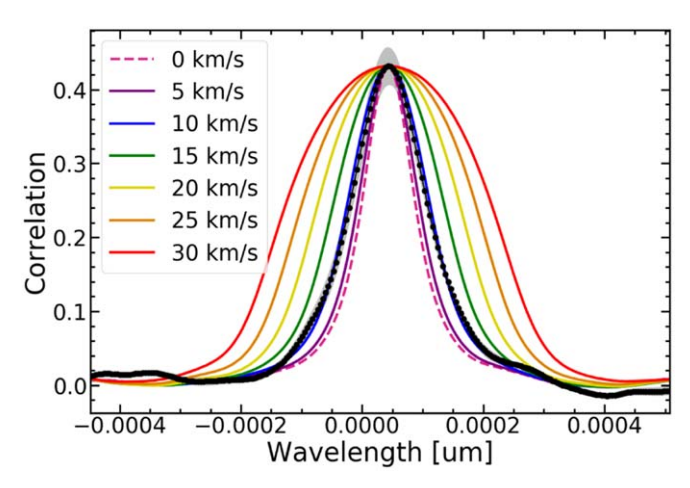


Figure 3. CCF between orders 4–19 (1.99–2.42 μ m) of the observed spectrum with a model atmosphere broadened to the instrumental resolution (black points), shown with 1σ uncertainties shaded in gray calculated using jackknife resampling technique. The CCFs between a model atmosphere broadened to the instrumental resolution, and that same model additionally broadened by a series of rotation rates (0, 5, 10, 15, 20, 25, 30 km s⁻¹) are shown in color.

Table 1 Model Tests and Resulting $v \sin i$'s

Model	v sin i
Original	$9.53 \pm 0.24 \ \mathrm{km \ s^{-1}}$
1580 K, 3.5 dex	$9.88 \; (+0.25 \; -0.24)$
1580 K, 4.5 dex	8.85 ± 0.22
2060 K, 3.5 dex	$9.89 \ (+0.23 \ -0.26)$
2060 K, 4.5 dex	$9.20 \; (+0.22 \; -0.21)$
0.25× solar C/O	$9.63 \ (+0.24 \ -0.23)$
0.5× solar C/O	9.69 (+0.28 -0.24)
1.5× solar C/O	8.73 (+0.25 -0.20)
0.1×P	9.87 (+0.20 -0.22)
$10\times P$	8.84 (+0.33 -0.28)

with the same instrumental resolution leads to less rotational line broadening and a correspondingly smaller $v \sin i$. To test our pressure broadening assumptions, we run two models with modified molecular opacities, where molecular cross sections were $10 \times$ and $0.1 \times$ the actual pressure for the whole profile. This simulates a scenario where pressure broadening parameters that are used to create the molecular cross sections are off by an order of magnitude. Collision-induced opacity of hydrogen and helium is treated separately for all models, using the standard pressure for each layer. When we recalculate $v \sin i$ values using these new models, we find that for the $0.1 \times$ model (which underpredicts the amount of pressure broadening) the resulting rotation rate is only 1.0σ away from the original value, and the $10\times$ model (which overpredicts pressure broadening) produces a $v \sin i$ that is 1.7σ lower (see Table 1). Both values are consistent with the original rotation rate measurement.

3.2. Measuring $P_{rot,p}$ for HD 106906 b

Periodic features in substellar light curves can be produced by cloud patchiness or planetary-scale waves, which manifest as longitudinal bands produced by zonal circulation (Apai et al. 2017, 2021). Lower-gravity objects typically have higher variability amplitudes and higher intrinsic-variability rates (Metchev et al. 2015; Vos et al. 2019). This observed variability appears to be

impacted by viewing geometry—more highly inclined objects (i.e., closer to pole on) have more attenuated brightness changes (Vos et al. 2017).

The photometric rotation period for HD 106906 b was published by Zhou et al. (2020). The authors used the Hubble Space Telescope Wide Field Camera 3 (WFC3) near-IR channel in time-resolved direct imaging mode to observe HD 106906 b in three bands: F127M, F139M, and F153M. Using techniques such as two-roll differential imaging and hybrid point-spread function modeling yielded $\sim\!\!1\%$ precision in the light curves across all three bands. Fitting the light curve with a sinusoid results in a period of 4.1 ± 0.3 hr and an amplitude of $0.49\%\pm0.12\%$.

Zhou et al. (2020) present several caveats to the rotation period measurement. First, they find only marginal evidence of variability, with a significance of 2.7σ . Because of this tentative detection, when fitting the light curves the authors applied a strict sinusoidal shape to the photometric modulations, and could not investigate whether the light curve could have multiple peaks. Previously, Apai et al. (2017) found that for 3 L/T transition brown dwarfs with high signal-to-noise data and extremely long baselines (>1 yr), the power spectra of their light curves produced peaks at both the full rotation period of the object as well as half the rotation period. A more recent analysis of long-baseline high-S/N photometry of Luhman 16 A and B found a similar result, with peaks at both the full and half rotation period (Apai et al. 2021). While this raises the question of whether the detected 4 hr rotation period of HD 106906 b is the full or half rotation period, both higher quality and theoretical light curves of brown dwarfs show that the full rotation period dominates the signal in the power spectrum for a given light curve (Zhang & Showman 2014; Apai et al. 2017, 2021). In addition, periodicity in the light curves of Jupiter and Neptune correspond to their full rotation periods (Karalidi et al. 2015; Simon et al. 2016; Ge et al. 2019). We thus assume that the full rotation period of HD 106906 b is 4.1 ± 0.3 hr.

Another caveat to this rotation period measurement is that photometric modulations for HD 106906 b are only detected in the bluest band (F127M), and not in the other two bands. However, for the majority of substellar objects, rotational modulations are wavelength dependent and have higher amplitudes at shorter (bluer) wavelengths (e.g., Apai et al. 2013; Yang et al. 2015; Zhou et al. 2016, 2019). Assuming a similar wavelength dependence for the photometric modulations in HD 106906 b as measured for 2M1207 b (Zhou et al. 2016), the closest spectral type young companion analog to HD 106906 b with detected modulation, the authors predict that the modulation amplitude for the redder bands would have been too small for them to observe. The detection of modulation in only the bluest band is therefore consistent with low overall amplitude variability and wavelength dependent modulations.

3.3. Measuring i_0

Given the wide projected separation of HD 106906 b (737 au), detecting orbital motion and placing constraints on orbital parameters requires long-baseline precision astrometry (e.g., Bowler et al. 2020). Recently, Nguyen et al. (2021) detected orbital motion of this companion using 14 yr of astrometry measurements between 2004 and 2017. All data were taken with HST using a combination of the Advanced Camera for Surveys, the Space Telescope Imaging Spectrograph, and the WFC3. By cross registering background star locations in the

HST images with the Gaia astrometric catalog, Nguyen et al. (2021) calculated astrometry to high precision (at the subpixel level). To obtain constraints on the orbital parameters of HD 106906 b, the authors used the open-source Python package orbitize! (Blunt et al. 2020) to perform an orbit fit to the assembled astrometric measurements. The line-of-sight orbital inclination i_o from these fits is $56^{+12\circ}_{-21}$. In this paper we use the posterior distribution shown in Figure 10 of Nguyen et al. (2021) when incorporating i_o in our analyses.

3.4. Measuring id

Scattered light imaging of the debris disk in the HD 106906 system with both GPI and SPHERE constrained the morphology of the disk (Kalas et al. 2015; Lagrange et al. 2016). In Lagrange et al. (2016), the disk detection with SPHERE was modeled using the GRATER code (Augereau et al. 1999) as an optically thin, inclined ring centered on the host binary. The authors assumed a dust density distribution that peaks at radius r_0 and has a power-law slope of $\alpha_{\rm in}$ inside of r_0 and $\alpha_{\rm out}$ outside of r_0 . In addition to r_0 and α_{out} , fitted model parameters include the inclination of the disk i_d , the position angle (PA), a scaling factor to match the total flux of the disk, and the Henyey-Greenstein coefficient g, which quantifies how anisotropic the scattering is. With this modeling, the authors find a disk inclination $i_d = 85^{\circ}.3 \pm 0^{\circ}.1$. In Kalas et al. (2015), the authors estimate a disk inclination of $i_d \sim 85^{\circ}$ by assuming the disk is circular and translating the disk aspect ratio from their fitted semimajor and minor axes to line-of-sight inclination. Because it is unclear whether the disk is rotating in a prograde or retrograde fashion, there is a degeneracy in i_d and Ω_d pairs, where Ω_d is the PA of the ascending node. Thus angles $(i_d = 85^\circ, \ \Omega_d = 104^\circ)$ and $(i_d = 95^\circ, \ \Omega_d = 284^\circ)$ are equally likely. In this paper, we assume a bimodal distribution for i_d , with $i_d = 85^{\circ}.3 \pm 0^{\circ}.1$ and $i_d = 94^{\circ}.7 \pm 0^{\circ}.1$ defining the two Gaussian distributions.

3.5. Measuring i_p

We combine P_{rot} and our measurement of $v \sin i$ to determine the line-of-sight spin axis inclination of the companion i_p . However, simply computing the inclination as:

$$\sin i = \left(\frac{v \sin i}{2\pi R/P_{\text{rot}}}\right) \tag{3}$$

does not account for correlations between relevant parameters (Masuda & Winn 2020). For example, v and $v \sin i$ are not statistically independent given that $v \sin i$ is always less than v. We therefore follow the method described in detail in Masuda & Winn (2020) and summarized for the application to HD 106906 b below.

Given v as the equatorial rotational velocity and $u = v \sin i$ as the projected rotation rate, we have the following two likelihood functions:

$$L_{\nu}(\nu) = p(d_{\nu}|\nu) \tag{4}$$

$$L_u(u) = p(d_u|u) \tag{5}$$

where d_v and d_u are the data sets from which these likelihood functions are calculated. In our case, $L_u(u)$ is the probability distribution for $v \sin i$ that we determined from our high-resolution

spectra, a Gaussian with peak location $9.5 \, \mathrm{km \, s^{-1}}$ and standard deviation $0.2 \, \mathrm{km \, s^{-1}}$. $L_{\nu}(\nu)$ is the probability distribution for ν , which we calculate using $\nu = 2\pi R/P_{\mathrm{rot}}$. For the radius R we calculate the effective blackbody radius:

$$R = \sqrt{\frac{L}{4\pi\sigma_b T_{\rm eff}^4}},\tag{6}$$

where L is the bolometric luminosity $\log (L_{\rm bol}/L_{\odot}) = -3.65 \pm 0.08$, σ_b is the Stefan–Boltzmann constant, and $T_{\rm eff}$ is the effective temperature $T_{\rm eff} = 1820 \pm 240$ K (Daemgen et al. 2017). This yields a radius of $1.49^{+0.37}_{-0.45}$ R_{Jup}. We produce a probability distribution for ν by incorporating uncertainties on $P_{\rm rot}$, $\log (L_{\rm bol}/L_{\odot})$, and $T_{\rm eff}$ in a Monte Carlo fashion.

With $L_u(u)$ and $L_v(v)$ in hand, Masuda & Winn (2020) specify two key assumptions:

1. d_v and d_u are independent, so the likelihood function for $D = \{d_v, d_u\}$ is separable:

$$L_{vu}(v, u) = p(D|v, u) = p(d_v|v, u) = p(d_v|v)p(d_u|u) = L_v(v)L_u(u);$$
(7)

2. v and i are a priori independent, which means that the prior $P_{vi}(v, i)$ is separable:

$$P_{vi}(v, i) = P_v(v)P_i(i) \tag{8}$$

and

$$p(v|i) = P_v(v); p(i|v) = P_i(i).$$
 (9)

Given these assumptions, the posterior distribution function (PDF) for $\cos i$ can be written as:

$$p(\cos i|D) \propto P_{\cos i}(\cos i) \int L_{\nu}(\nu) L_{u}(\nu \sqrt{1 - \cos^{2} i}) P_{\nu}(\nu) d\nu.$$
(10)

where $P_{\cos i}(\cos i)$ is uniform between 0 and 1 and the prior on the rotation rate $P_{\nu}(\nu)$ is uniform from 0 to break-up speed.

Converting this PDF in $\cos i$ to a PDF in i yields the distribution shown in Figure 4. We note that the posterior distribution for i_p is bimodal and symmetric around 90° simply because we do not know whether this spin axis vector (which has directionality) is pointed toward us or away from us. Therefore the mode and 68% highest probability density interval (HPDI) of i_p is $14^\circ \pm 4^\circ$ for $i_p < 90^\circ$, and $166^\circ \pm 4^\circ$ for $i_p > 90^\circ$.

3.6. Measuring the 3D Spin-Orbit Architecture of the HD 106906 b System

Our goal is to measure the true 3D angles between the three angular momentum vectors in this system—the companion spin axis, the companion orbit normal, and the disk normal. These angles are given by:

$$\Psi_{\rm op} = \cos^{-1}(\cos i_p \cos i_o + \sin i_p \sin i_o \cos(\Omega_o - \Omega_p)) \quad (11)$$

$$\Psi_{\rm dp} = \cos^{-1}(\cos i_p \cos i_d + \sin i_p \sin i_d \cos(\Omega_d - \Omega_p)) \quad (12)$$

$$\Psi_{\rm od} = \cos^{-1}(\cos i_d \cos i_o + \sin i_d \sin i_o \cos(\Omega_o - \Omega_d)) \quad (13)$$

where $\Psi_{\rm op}$ is the true companion obliquity, $\Psi_{\rm dp}$ is the true spindisk mutual inclination, and $\Psi_{\rm od}$ is the true orbit-disk mutual inclination. The PAs Ω_o , Ω_d , and Ω_p measure how the orbit, disk, and companion spin axis, respectively, are oriented on the sky plane. The nodal angle Ω_p is unknown.

https://github.com/sblunt/orbitize

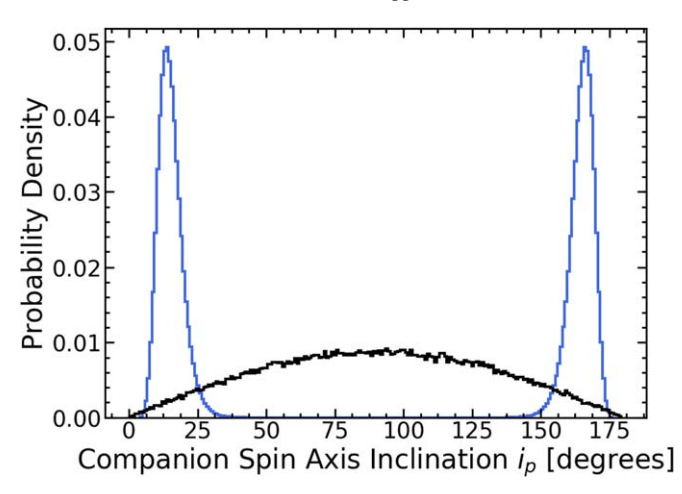


Figure 4. Normalized posterior distribution of the line-of-sight companion spin axis inclination i_p (blue). This distribution is bimodal and symmetric around 90° because we do not know whether this spin axis vector (which has directionality) is pointed toward us or away from us. Setting aside the symmetric distribution above 90°, just considering values of $i_p < 90^\circ$ we find that the mode and 68% highest probability density interval of i_p are $14^\circ \pm 4^\circ$. This distribution is compared to a random inclination distribution (black) whose values are drawn from a uniform distribution in $\cos i$.

The difference between the line-of-sight inclination of the companion spin axis i_p and that of the orbit normal i_o yields a lower limit on the true deprojected obliquity Ψ_{op} (Bowler et al. 2017):

$$\Psi_{\rm op} > |i_p - i_o|. \tag{14}$$

Similarly:

$$\Psi_{\rm dp} > |i_p - i_d| \tag{15}$$

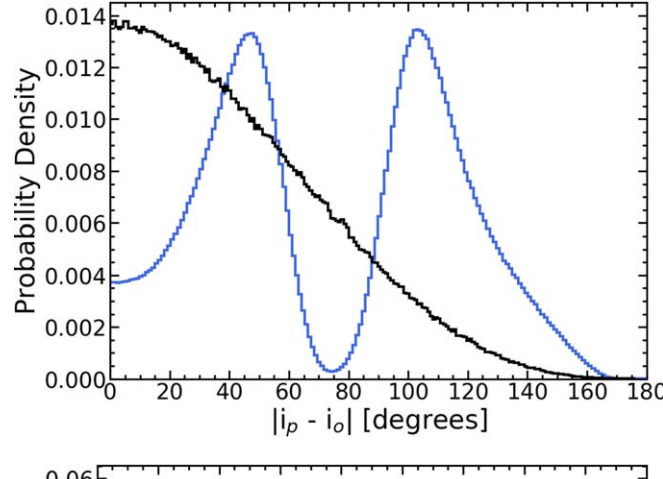
$$\Psi_{\rm od} > |i_o - i_d|. \tag{16}$$

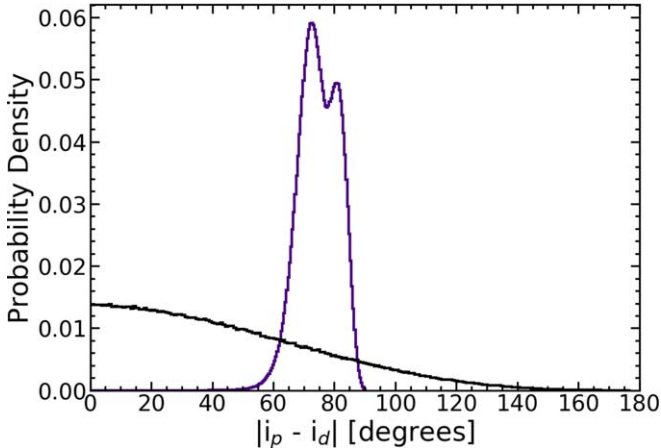
Figure 5 shows the posteriors for $|i_p-i_o|$, $|i_p-i_d|$, and $|i_o-i_d|$. We also plot a random distribution in black for comparison, where i_p , i_o , and i_d are all drawn from uniform distributions in $\cos i$. We find that the 68% HPDI for $|i_p-i_o|$ lies between [32°, 119°]. For $|i_o-i_d|$ the 68% HPDI is [16°, 48°], and for $|i_p-i_d|$ we have the tightest 68% HPDI of [69°, 83°].

Since these projected angles are all lower limits on the true 3D angles, we can say that our results tend to favor more "misaligned" orientations (defined here as mutual inclinations of 20°–180°). A schematic illustration of the line-of-sight architecture of the system is shown in Figure 6.

We now calculate full probability distributions for all Ψ 's using Equations (11)–(13). For Equations (11) and (12) we assume Ω_p is randomly drawn from a uniform distribution between 0 and 2π . For Equation (13), both Ω_o and Ω_d have been measured: $\Omega_o=99^{+26\circ}_{-28}$ or $279^{+25\circ}_{-29}$, and $\Omega_d=104^\circ.4\pm0^\circ.3$ or $284^\circ\pm0^\circ.3$ (Kalas et al. 2015; Lagrange et al. 2016; Nguyen et al. 2021). Figure 7 shows the resulting probability distributions for $\Psi_{\rm op},\Psi_{\rm dp},$ and $\Psi_{\rm od},$ along with a random mutual inclination distribution $\Psi_{\rm random}$ in black for reference.

Not knowing Ω_p along with poor constraints on HD 106906 b's orbital elements (a consequence of the companion's wide orbital separation) leads to broad posterior distributions for the true deprojected angles $\Psi_{\rm op}$ and $\Psi_{\rm od}$. By comparison, Ψ_{pd} is remarkably well constrained. All of these posteriors are bimodal, reflecting symmetries across 90°. For each Ψ posterior we calculate the mode and 68% HPDI for each half of the distribution below and above 90°. We find that the true companion obliquity





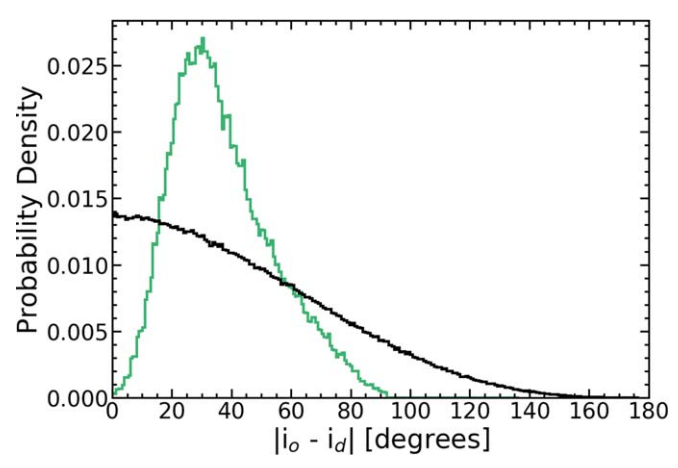


Figure 5. Top panel: posterior distribution for the line-of-sight projected companion obliquity (blue), which has a 68% HPDI of [32°, 119°]. Middle panel: posterior distribution for the line-of-sight projected spin-disk angle (purple), which has a 68% HPDI of [69°, 83°]. Bottom panel: posterior distribution for the line-of-sight projected orbit-disk angle, which has a 68% HPDI of [16°, 48°]. These line-of-sight projections are lower limits on the true 3D mutual inclinations $\Psi_{\rm op}$, $\Psi_{\rm dp}$, and $\Psi_{\rm od}$. The posterior distributions are compared to a random projected inclination distribution (black), where i_o , i_d , and i_p have all been drawn from uniform distributions in $\cos i$.

 $\Psi_{\rm op}$ is $55^{+22\circ}_{-16}$ or $125^{+16\circ}_{-22}$, the true spin-disk angle $\Psi_{\rm dp}$ is $84^{+6\circ}_{-8}$ or $96^{+8\circ}_{-6}$, and the true mutual inclination between the orbit and disk normals $\Psi_{\rm od}$ is $39^{+20\circ}_{-15}$ or $141^{+15\circ}_{-20}$ (Table 2). Each of these deprojected mutual inclinations deviates distinctly from the geometric prior–both $\Psi_{\rm op}$ and $\Psi_{\rm od}$ favor angles away from 90° , which is where the geometric prior peaks, and while $\Psi_{\rm dp}$ peaks

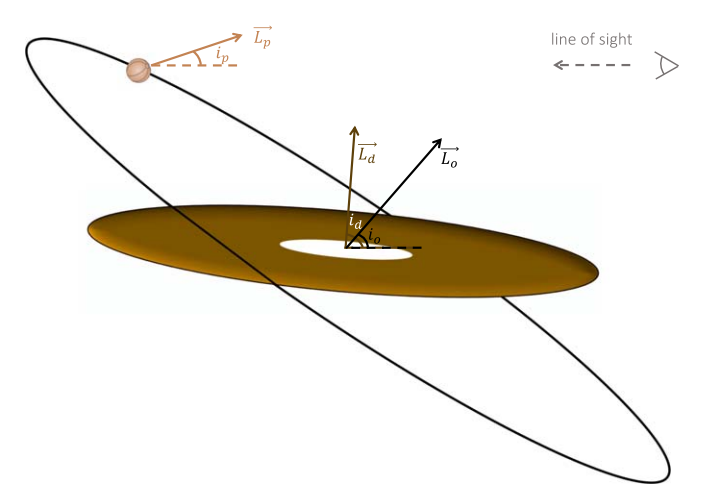


Figure 6. 3D architecture of the HD 106906 system showing how each of the three angular momentum vectors, namely L_p for the companion spin, L_o for the orbit, and L_d for the debris disk, are oriented along our line of sight, with corresponding angles i_p , i_o , and i_d . Both i_p and i_d are symmetric around 90° (L_p and L_d could be pointing toward or away from us). Mutual inclinations between each set of vectors favor misalignment. Note the purpose of this figure is to illustrate the orientation of the three angular momentum vectors—it does not accurately depict other separate system properties (i.e., disk asymmetry, disk inner and outer radius; see Figure 9 in Nguyen et al. 2021 for a scattered light image of the system showing some of these properties).

around 90° it is a much tighter constraint than a random distribution.

We quantify the probability that each Ψ distribution yields an "aligned" state, which we define as $\Psi \in (0^\circ, 20^\circ)$, or a "misaligned" state where $\Psi \in (20^\circ, 180^\circ)$. The Bayesian odds ratio is p(m|D)/p (a|D), where p(m|D) is the probability of misaligned state m given data D, and p(a|D) is the probability of an aligned state a. The former probability is the integral of the posterior distribution $p(\Psi|D)$ (the colored histograms in Figure 7) from $20^\circ-180^\circ$, while the latter probability is obtained by integrating the posterior distribution from $0^\circ-20^\circ$.

We compute these integrals over the posterior distributions for all three mutual inclinations Ψ_{op} , Ψ_{dp} , and Ψ_{od} , as well as for the geometric prior distribution which is uniform in $\cos \Psi_{\rm random}$ (Figure 7, black curve). In the absence of any data, the geometric prior yields an odds ratio favoring misalignment to alignment at 32:1 (2.2 σ). The odds ratios for the true companion obliquity Ψ_{op} and the orbit-disk mutual inclination Ψ_{od} are only slightly larger, 39:1 (2.3 σ) and 40:1 (2.3 σ), respectively. Nevertheless, the fact that the shapes of both posteriors differ significantly from that of the prior indicates that the odds favoring misalignment for both Ψ_{op} and Ψ_{od} are not entirely driven by the prior. We can say there is tentative evidence that both of these mutual inclinations are large. By comparison, the true spin-disk angle Ψ_{dp} has an odds ratio that favors misalignment much more strongly than does our random prior–97081:1 (4.4 σ). We can say with confidence that this system contains an edge-on disk and a planet spinning nearly pole on; even allowing for sky-plane degeneracy, our measurements indicate that the companion spin axis and disk normal are strongly misaligned.

4. Discussion: Possible Formation Histories

For the HD 106906 system, we have strong evidence that the spin axis of the planetary-mass companion (PMC) and the orbit normal of the debris disk are misaligned. In addition, we find

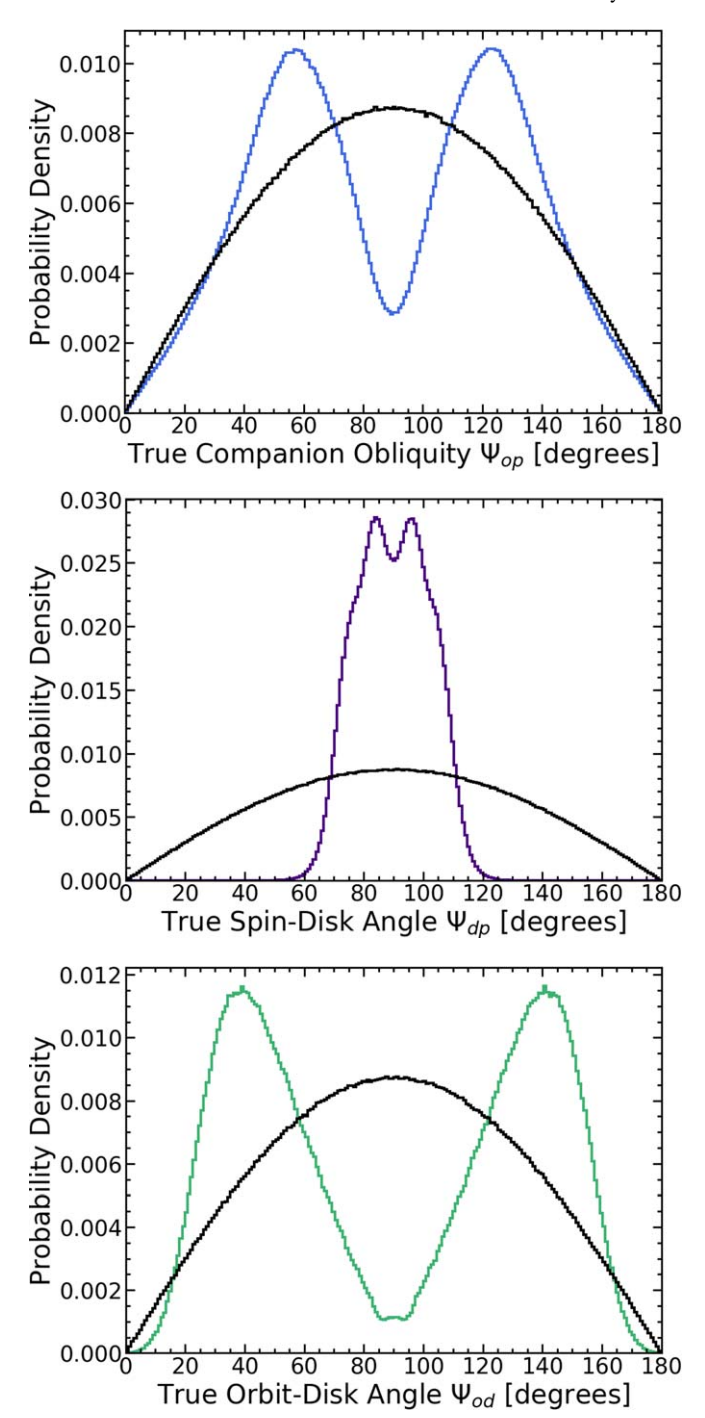


Figure 7. Top panel: normalized posterior distribution for the true companion obliquity $\Psi_{\rm op}$ (blue). Middle panel: normalized posterior distribution for the true spin-disk angle $\Psi_{\rm dp}$ (purple). Bottom panel: normalized posterior distribution for the true orbit-disk angle $\Psi_{\rm od}$ (green). These posterior distributions are compared to geometrically random mutual inclination distributions (black).

tentative evidence that the true PMC obliquity, and the mutual inclination between the PMC orbit and debris disk, are large. We proceed on the assumption that all three vectors are mutually misaligned and consider possible origin scenarios.

As in the case of 2M0122 b, gravitational instability in a turbulent environment is a promising way to create tilted architectures. The setting can either be a gravito-turbulent disk around a protostar (Bryan et al. 2020b; Jennings & Chiang 2021), or a portion of a self-gravitating turbulent cloud that fragments

Table 2
Measured Parameters

Parameter	Measured Value	Ref
$v_p \sin i_p$	$9.5 \pm 0.2~{\rm km~s}^{-1}$	This work
$P_{\text{rot},p}$	$4.1\pm0.3~\mathrm{hr}$	Zhou et al. (2020)
i_p	$14^{\circ} \pm 4^{\circ}$ or $166^{\circ} \pm 4^{\circ}$	This work
$i_p \ i_o$	56^{+12}_{-21}	Nguyen et al. (2021)
i_d	85.3 ± 0.1 or 94.7 ± 0.1 deg	Kalas et al. (2015), Lagrange
		et al. (2016)
$ i_o - i_p $	(32°, 119°)	This work
$ i_p - i_d $	(69°, 83°)	This work
$ i_d - i_o $	(16°, 48°)	This work
$\Psi_{ m op}$	55^{+22}_{-16} ° or 125^{+16}_{-22} °	This work
$\Psi_{ m dp}$	$84^{+6\circ}_{-8}$ or $96^{+8\circ}_{-6}$	This work
$\Psi_{ m od}$	39^{+20}_{-15} or 141^{+15}_{-20}	This work

Note. The three i inclinations presented here are all along our line of sight. The angle i_p is symmetric about 90° due to the fact that we do not know whether this spin angular momentum vector is pointing toward us or away from us. The angle i_d has two solutions because it is unclear whether the disk is rotating prograde or retrograde, so there are two combinations of i_d and Ω_d , where Ω_d is the PA of the ascending node, that are equally likely. The line-of-sight mutual inclinations $|i_o-i_p|,\ |i_p-i_d|,\$ and $|i_d-i_o|$ are lower limits on the true deprojected angles $\Psi_{\rm op},\ \Psi_{\rm dp},\$ and $\Psi_{\rm od}.$ Here we quote the mode and 68% highest probability density intervals for these angles.

into a binary (e.g., Bate et al. 2002; Bate 2009, 2018). Turbulent eddies spin in a variety of directions, and when those eddies gravitationally collapse, the objects they form should have a correspondingly wide range of spin directions. In situ formation of HD 106906 b in a disk would require a nebula as large as 1000 au in radius; Class I disks range up to this size (Maury et al. 2019, see their Figure 9). Numerical simulations of fragmenting gravitoturbulent disks by Jennings & Chiang (2021) find that obliquities of nascent fragments can be as high as 45°, and that subsequent collisions between fragments can raise or lower obliquities. Turbulence also imparts vertical velocities to disk fragments, driving them out of the midplane; orbital inclinations up to 20° are suggested by these simulations. In population synthesis calculations by Bate (2018) of stellar binaries fragmenting from a turbulent cloud, roughly 2/3 of circumstellar disks are inclined by more than 30° relative to the binary orbit, for binaries with semimajor axes between 100 and 1000 au (see their Figure 20). This result of frequent disk-orbit misalignments, in combination with their finding that most (80%) of stellar spin axes are within \sim 45° of circumstellar disk normals (their Figure 23), would seem to imply that spin-orbit angles are typically large (obliquities are not explicitly calculated in Bate 2018). In sum, all the misalignments indicated by our observations seem possible to account for by turbulent gravitational instability.

Another scenario is that the PMC formed as an isolated object via molecular cloud fragmentation and was subsequently captured by a star. Binaries can form in fly-by events if sufficient energy is dissipated during the encounter; circumstellar disks can provide this energy sink (e.g., Clarke & Pringle 1991a, 1991b; Moeckel & Bally 2006; Offner et al. 2016; Bate 2018). Assuming the disk surrounding the stellar host is the dominant sink (as opposed to any smaller and less massive disk orbiting the PMC), we have no reason to expect the planet's spin axis to be aligned with its orbit normal or the disk normal. The captured PMC's orbital plane may also be randomly oriented with respect to the circumstellar disk plane, at least initially; this is borne out in simulations by

Bate (2018, see their Figure 22). However, these simulations lasted only up to $\sim 10^5$ yr; on longer timescales the PMC orbit could be gravitationally torqued into alignment with the circumstellar disk. Thus two if not three misalignments can be accommodated in this encounter scenario.

A handful of other mechanisms can produce only one or two of the three possibly large mutual inclinations observed in this system. A stellar fly-by can tilt the orbit of the PMC, generating a large obliquity as well as a mutual inclination between the orbit and disk planes (e.g., Laughlin & Adams 1998; Kenyon & Bromley 2004; Zakamska & Tremaine 2004; Parker & Quanz 2012; De Rosa & Kalas 2019). However, the PMC spin axis is not expected to be materially altered by the fly-by, and thus the observed misalignment between the spin axis and the disk normal in HD 106906 is unexplained in this scenario. Another way to generate obliquity is by using the stellar tidal potential to tilt a circumplanetary disk and by extension its host planet (Lubow & Ogilvie 2000; Martin & Armitage 2021). This scenario does not address the misalignment between the orbit and disk normals.

5. Conclusions

In this study we constrained the orientation of the planetary spin, orbital, and disk angular momentum vectors for the HD 106906 system. HD 106906 is a 13 ± 2 Myr system in ScoCen composed of a close binary of two F stars, a widely separated planetary-mass tertiary 106906 b, and an asymmetric debris disk interior to companion b's orbit. Line-of-sight inclinations for the companion orbit i_o and debris disk i_d were previously published (Kalas et al. 2015; Lagrange et al. 2016; Nguyen et al. 2021). The debris disk is known to be viewed edge on. Here we measured the line-of-sight inclination of the companion spin axis i_p . We used near-IR high-resolution spectra from IGRINS/Gemini South to measure rotational line broadening for HD 106906 b, and found a rotation rate of $9.5 \pm 0.2 \,\mathrm{km \, s^{-1}}$. Combining this measurement with the photometric rotation period yielded a companion spin axis inclination of $14^{\circ} \pm 4^{\circ}$ (when considering inclinations $< 90^{\circ}$). We are seeing this companion nearly pole on (Figure 6).

Differences between line-of-sight inclinations yield lower limits on the true 3D mutual inclinations. We computed the projected inclinations $|i_o - i_p|$, $|i_p - i_d|$, and $|i_d - i_o|$. The projected companion obliquity $|i_o - i_p|$ has a 68% highest probability density interval (HPDI) of [32°, 119°]. The projected orbit-disk angle $|i_d - i_o|$ has an HPDI of [16°, 48°]. The projected spin-disk inclination $|i_p - i_d|$ is the most strongly constrained, with an HPDI of [69°, 83°]. These lower limits on the 3D mutual inclinations favor more "misaligned" orientations (defined here as mutual inclinations of 20°–180°).

We further constrained the true 3D mutual inclinations between the companion spin, companion orbit, and disk angular momentum vectors: $\Psi_{\rm op}$ (true companion obliquity), $\Psi_{\rm dp}$ (true spin-disk mutual inclination), and $\Psi_{\rm od}$ (true orbit-disk angle). Since we have no constraints on the companion spin axis orientation in the sky plane, to compute distributions for $\Psi_{\rm op}$ and $\Psi_{\rm dp}$ we assumed that nodal angle Ω_p was randomly and uniformly distributed between 0 and 2π (see Equations (11) and 12). To calculate a distribution for $\Psi_{\rm od}$ we used measured values of Ω_d and Ω_o for the disk and orbit, respectively (see Equation (13)).

The lack of a constraint on how the companion spin axis is oriented in the sky plane combined with poor constraints on HD 106906 b's orbit (given its wide projected separation) leads to broad posterior distributions for Ψ_{op} and Ψ_{od} , whereas Ψ_{dp} is

more tightly constrained (Figure 7). Since these posteriors are bimodal (given symmetries about 90°), we calculated the mode and 68% HPDI for each Ψ both above and below 90° . We found that Ψ_{op} is $55^{+22\circ}_{-16}$ or $125^{+16\circ}_{-22}$, Ψ_{dp} is $84^{+6\circ}_{-8}$ or $96^{+8\circ}_{-6}$, and Ψ_{od} is $39^{+20\circ}_{-15}$ or $141^{+15\circ}_{-20}$. All three angles exhibit marked differences from the geometric prior, with Ψ_{op} and Ψ_{od} peaking at values away from the 90° maximum of the geometric prior, and Ψ_{dp} showing a much tighter distribution around 90° than the prior.

We assessed how likely the three angular momentum vectors were to be "misaligned" or "aligned" (defined as mutual inclinations between $20^{\circ}-180^{\circ}$ and $0^{\circ}-20^{\circ}$, respectively) by calculating an odds ratio for each angle. Both the true obliquity $\Psi_{\rm op}$ and mutual inclination between the orbit and the disk $\Psi_{\rm od}$ tentatively favor misalignment with ratios of 39:1 (2.3 σ) and 40:1 (2.3 σ), respectively. The orientation between the disk normal and the companion spin axis $\Psi_{\rm dp}$ strongly favors misalignment at 97081:1 odds (4.4 σ). We are seeing an edgeon disk orbited by a planet spinning nearly pole on.

Given strong evidence that the PMC spin axis and disk normal are misaligned, and tentative evidence that the true PMC obliquity and the mutual inclination between the PMC orbit and debris disk are large, we considered various origin scenarios. As in the case of 2M0122 b (Bryan et al. 2020b), gravitational instability in a turbulent medium, either in a circumstellar disk or cloud setting, is viable. Gravitational collapse of turbulent eddies naturally yields large obliquities, and subsequent fragment interactions (collisions and mergers) can further increase obliquity dispersions (Jennings & Chiang 2021). Disk turbulence also excites nonzero orbital inclinations. In simulations of binary star fragmentation in a turbulent molecular cloud, disks and binary orbits are frequently misaligned, especially for wide binaries (Bate 2018). Thus all observed misalignments in HD 106906 are potentially accounted for in a turbulent gravitational instability scenario. Another possibility is that the PMC formed via molecular cloud fragmentation initially isolated and unbound from the star, and was subsequently captured by the star in a dissipative fly-by event. In this encounter scenario there is no reason to expect the PMC's spin axis would be aligned with its orbit normal or the disk normal, and the orbital plane could also be randomly oriented with respect to the disk plane. In all of the above scenarios, HD 106906 b forms top down by gravitational instability, and thus shares kinship with stars.

This is only the second obliquity constraint for a PMC outside the Solar System. The work of measuring a planet's rotation speed, spin period, and 3D orbit remains challenging. But the insights into planet formation enabled by obliquity are new, powerful, and unique. The bane of sky-plane degeneracies may be banished by a larger sample of systems like 2M0122 b and HD 106906 b, which will enable statistical constraints.

We thank Ian Czekala, Gaspard Duchene, and Yifan Zhou for helpful conversations. M.L.B. is supported by the Heising-Simons Foundation 51 Pegasi b Fellowship. C.V.M. acknowledges the support of the National Science Foundation grant number 1910969. B.P.B. acknowledges support from the National Science Foundation grant AST-1909209 and NASA Exoplanet Research Program grant 20-XRP20_2-0119.

Based on observations obtained at the international Gemini Observatory, a program of NSFs NOIRLab, which is managed by the Association of Universities for Research in Astronomy (auRA) under a cooperative agreement with the National Science Foundation. On behalf of the Gemini Observatory partnership: the National Science Foundation (United States), National Research Council (Canada), Agencia Nacional de Investigación y Desarrollo (Chile), Ministerio de Ciencia, Tecnología e Innovación (Argentina), Ministério da Ciência, Tecnologia, Inovações e Comunicações (Brazil), and Korea Astronomy and Space Science Institute (Republic of Korea). This work used the Immersion Grating Infrared Spectrometer (IGRINS) that was developed under a collaboration between the University of Texas at Austin, and the Korea Astronomy and Space Science Institute (KASI), with the financial support of the Mt. Cuba Astronomical Foundation, of the US National Science Foundation under grants AST-1229522 and AST-1702267, of the McDonald Observatory of the University of Texas at Austin, of the Korean GMT Project of KASI, and Gemini Observatory.

ORCID iDs

Marta L. Bryan https://orcid.org/0000-0002-6076-5967
Eugene Chiang https://orcid.org/0000-0002-6246-2310
Caroline V. Morley https://orcid.org/0000-0002-4404-0456
Gregory N. Mace https://orcid.org/0000-0001-7875-6391
Brendan P. Bowler https://orcid.org/0000-0003-2649-2288

References

```
Ackerman, A. S., & Marley, M. S. 2001, ApJ, 556, 872
Apai, D., Karalidi, T., Marley, M. S., et al. 2017, Sci, 357, 683
Apai, D., Nardiello, D., & Bedin, L. R. 2021, ApJ, 906, 64
Apai, D., Radigan, J., Buenzli, E., et al. 2013, ApJ, 768, 121
Augereau, J. C., Lagrange, A. M., Mouillet, D., Papaloizou, J. C. B., &
   Grorod, P. A. 1999, A&A, 348, 557
Bailey, V., Meshkat, T., Reiter, M., et al. 2014, ApJL, 780, L4
Bate, M. R. 2009, MNRAS, 392, 590
Bate, M. R. 2018, MNRAS, 475, 5618
Bate, M. R., Bonnell, I. A., & Bromm, V. 2002, MNRAS, 332, L65
Blunt, S., Wang, J., Angelo, I., et al. 2020, AJ, 159, 89
Bowler, B. P. 2016, PASP, 128, 102001
Bowler, B. P., Blunt, S. C., & Nielsen, E. L. 2020, AJ, 159, 63
Bowler, B. P., Kraus, A. L., Bryan, M. L., et al. 2017, AJ, 154, 165
Bowler, B. P., Liu, M. C., Shkolnik, E. L., & Dupuy, T. J. 2013, ApJ, 774, 55
Bryan, M. L., Chiang, E., Bowler, B. P., et al. 2020b, AJ, 159, 181
Bryan, M. L., Ginzburg, S., Chiang, E., et al. 2020a, ApJ, 905, 37
Burrows, A., Marley, M., Hubbard, W. B., et al. 1997, ApJ, 491, 856
Clarke, C. J., & Pringle, J. E. 1991a, MNRAS, 249, 588
Clarke, C. J., & Pringle, J. E. 1991b, MNRAS, 249, 584
Correia, A. C. M. 2006, E&PSL, 252, 398
Czekala, I., Chiang, E., Andrews, S. M., et al. 2019, ApJ, 883, 22
Daemgen, S., Todorov, K., Quanz, S. P., et al. 2017, A&A, 608, A71
De Rosa, R. J., & Kalas, P. 2019, AJ, 157, 125
Dobrovolskis, A. R. 1980, Icar, 41, 18
Ge, H., Zhang, X., Fletcher, L. N., et al. 2019, AJ, 157, 89
Jennings, M., & Chiang, E. 2021, MNRAS, 507, 5187
Kalas, P. G., Rajan, A., Wang, J. J., et al. 2015, ApJ, 814, 32
Karalidi, T., Apai, D., Schneider, G., Hanson, J. R., & Pasachoff, J. M. 2015,
   ApJ, 814, 65
Kausch, W., Noll, S., Smette, A., et al. 2015, A&A, 576, A78
Kenyon, S. J., & Bromley, B. C. 2004, Natur, 432, 598
Lagrange, A. M., Langlois, M., Gratton, R., et al. 2016, A&A, 586, L8
Laskar, J., & Robutel, P. 1993, Natur, 361, 608
Laughlin, G., & Adams, F. C. 1998, ApJL, 508, L171
Lee, J.-J., & Gullikson, K. 2016, plp: v2.1 alpha 3, Zenodo, doi:10.5281/
  zenodo.56067
Li, G. 2021, ApJ, 915, L2
Lissauer, J. J., & Kary, D. M. 1991, Icar, 94, 126
Lubow, S. H., & Ogilvie, G. I. 2000, ApJ, 538, 326
Mace, G., Sokal, K., Lee, J.-J., et al. 2018, Proc. SPIE, 10702, 107020Q
```

```
Marley, M., Saumon, D., Morley, C., & Fortney, J. 2018, Sonora 2018: Cloud-free, solar composition, solar C/O substellar evolution models, Zenodo, doi:10.5281/zenodo.2628068
```

Marley, M., Saumon, D., Morley, C., et al. 2021, Sonora Bobcat: cloud-free, substellar atmosphere models, spectra, photometry, evolution, and chemistry Zenodo, doi:10.5281/zenodo.5063476

Marley, M. S., Gelino, C., Stephens, D., Lunine, J. I., & Freedman, R. 1999, ApJ, 513, 879

Martin, R. G., & Armitage, P. J. 2021, ApJL, 912, L16

Martin, R. G., Nixon, C., Lubow, S. H., et al. 2014, ApJL, 792, L33

Masuda, K., & Winn, J. N. 2020, AJ, 159, 81

Maury, A. J., André, P., Testi, L., et al. 2019, A&A, 621, A76

Metchev, S. A., Heinze, A., Apai, D., et al. 2015, ApJ, 799, 154

Millholland, S., & Batygin, K. 2019, ApJ, 876, 119

Millholland, S., & Laughlin, G. 2019, NatAs, 3, 424

Moeckel, N., & Bally, J. 2006, ApJ, 653, 437

Morley, C. V., Fortney, J. J., Marley, M. S., et al. 2012, ApJ, 756, 172

Nesvorný, D. 2018, ARA&A, 56, 137

Nguyen, M. M., De Rosa, R. J., & Kalas, P. 2021, AJ, 161, 22

Offner, S. S. R., Dunham, M. M., Lee, K. I., Arce, H. G., & Fielding, D. B. 2016, ApJL, 827, L11

```
Park, C., Jaffe, D. T., Yuk, I.-S., et al. 2014, Proc. SPIE, 9147, 91471D
Parker, R. J., & Quanz, S. P. 2012, MNRAS, 419, 2448
Reinhardt, C., Chau, A., Stadel, J., & Helled, R. 2020, MNRAS, 492,
Saumon, D., & Marley, M. S. 2008, ApJ, 689, 1327
Schlichting, H. E., & Sari, R. 2007, ApJ, 658, 593
Simon, A. A., Rowe, J. F., Gaulme, P., et al. 2016, ApJ, 817, 162
Smette, A., Sana, H., Noll, S., et al. 2015, A&A, 576, A77
Storch, N. I., Anderson, K. R., & Lai, D. 2014, Sci, 345, 1317
Touma, J., & Wisdom, J. 1993, Sci, 259, 1294
Vos, J. M., Allers, K. N., & Biller, B. A. 2017, ApJ, 842, 78
Vos, J. M., Biller, B. A., Bonavita, M., et al. 2019, MNRAS, 483, 480
Ward, W. R., & Hamilton, D. P. 2004, AJ, 128, 2501
Yang, H., Apai, D., Marley, M. S., et al. 2015, ApJL, 798, L13
Yuk, I.-S., Jaffe, D. T., Barnes, S., et al. 2010, Proc. SPIE, 7735, 77351M
Zakamska, N. L., & Tremaine, S. 2004, AJ, 128, 869
Zhang, X., & Showman, A. P. 2014, ApJL, 788, L6
Zhou, Y., Apai, D., Bedin, L. R., et al. 2020, AJ, 159, 140
Zhou, Y., Apai, D., Lew, B. W. P., et al. 2019, AJ, 157, 128
Zhou, Y., Apai, D., Schneider, G. H., Marley, M. S., & Showman, A. P. 2016,
```

ApJ, 818, 176